51st AIAA/ASME/ASCE/AHS/ASC Structures, Structural Dynamics, and Materials Conference
 18th
12 - 15 April 2010, Orlando, Florida

AIAA 2010-2887

Nonlinear Aeroelastic Simulations of a Flapping Wing Micro Air Vehicle Using Two Unsteady Aerodynamic Formulations

Weihua Su[1] and Carlos E. S. Cesnik[2]
The University of Michigan, Ann Arbor, MI, 48109-2140

Nonlinear aeroelasticity of a flapping wing Micro Air Vehicle (MAV) is analyzed in this paper. The geometrically nonlinear deformations are modeled by a nonlinear strain-based beam formulation, coupled with six rigid-body degrees of freedom of the aircraft. Wing flapping kinematics is described using a set of Euler angles. Two types of unsteady aerodynamic formulations are incorporated for loads on all lifting surfaces. One is Peters' finite-state inflow formulation and the other is developed in Cranfield University, which considers the effects of vortex shedding from both the airfoil's leading- and trailing-edges on lift generation. All these formulations are implemented in an integrated numerical frame-work, where coupled aeroelastic and flight dynamic simulations can be performed. The two aerodynamic formulations are prototyped within this framework and their applicability is assessed.

Nomenclature

$A_1 \sim A_{11}$	=	coefficients computed from the airfoil degrees of freedom
a	=	distance of beam reference axis (pitching axis) in front of mid-chord, m
a_0	=	local aerodynamic frame, with a_{0y} axis aligned with zero lift line of airfoil
a_1	=	local aerodynamic frame, with a_{1y} axis aligned with airfoil motion velocity
B	=	body reference frame
b	=	positions and orientations of the B frame, as time integral of β; semi-chord of airfoil, m
B_F, B_M	=	influence matrices for the distributed forces and moments
c	=	airfoil chord length, m
C_{FF}, C_{FB}, C_{BF}, C_{BB}	=	components of the generalized damping matrix
C^{GB}	=	rotation matrix from the B frame to the G frame
d	=	distance of mid-chord in front of beam reference axis, m
F_1, F_2, F_3	=	influence matrices in the inflow equations
F^{acc}, F^{cen}, F^{cor}, F^{int}	=	additional forces for flapping members due to the flapping motion
F^{dist}, F^{pt}	=	distributed and point forces
$\hat{F}$, $\hat{M}$	=	aerodynamic forces and moments calculated in the $\hat{\zeta}$ frame
G	=	global (inertial) reference frame
g	=	gravity acceleration, m/s^2
h	=	absolute positions and rotations of beam nodes
H_{hb}	=	matrix consisting of influence from Jacobian (J_{hb}) and body angular velocities (ω_B)
J	=	Jacobian matrix
K_{FF}	=	components of the generalized stiffness matrix
M, C, K	=	discrete mass, damping, and stiffness matrices of the whole system
M^{dist}, M^{pt}	=	distributed and point moments
M_{FF}, M_{FB}, M_{BF}, M_{BB}	=	components of the generalized mass matrix
N	=	influence matrix for the gravity force
P_B	=	inertia position of the B frame, resolved in the G frame
p_B, θ_B	=	position and orientation of the B frame, as time integral of v_B and ω_B, respectively
p_w	=	position of the w frame with respect to the B frame

[1] Post-doctoral Research Fellow (suw@umich.edu), Department of Aerospace Engineering, Senior Member, AIAA.
[2] Professor (cesnik@umich.edu), Department of Aerospace Engineering, Associate Fellow, AIAA.

R = generalized load vector
R_{af} = radius of the airfoil after transformed into the circular complex frame, $R_{af} = c/4$
s = beam coordinate, m
v_B, ω_B = linear and angular velocities of the B frame, resolved in the B frame itself
w = local beam reference frame defined at each node along beam reference line
$\dot{y}$, $\dot{z}$ = airfoil translational velocity components resolved in the a_0 frame, m/s
Z = complex coordinate system fixed to the airfoil, $Z = Re^{i\theta} = x + iy$

Greek letters

α = pitching angle of the airfoil, rad
$\dot{\alpha}$ = airfoil angular velocity about the a_{0x} axis, rad/s
β = body velocities, with translational and angular components, resolved in the B frame
Γ = circulation
γ = vorticity
Γ_0 = quasi-steady circulation
γ_0 = quasi-steady component of bound vorticity
γ_1 = wake induced bound vorticity
γ_b = total bound vorticity
γ_{fs} = bound vorticity due to free stream
γ_{lv} = vorticity due to wake from leading-edge
γ_{us} = bound vorticity unsteady motion of the airfoil
γ_{wk} = vorticity due to wake from trailing-edge
ε = elastic strain vector
ε^0 = initial (prescribed) elastic strain vector
ζ = rotating aerodynamic frame fixed at the mid-chord of airfoil
$\tilde{\zeta}$ = fixed (inertia) frame
$\hat{\zeta}$ = non-rotating aerodynamic frame fixed at the pitching axis
ζ_B = quaternions defining orientation of body frame (B)
Θ = commanded yaw-type (sweep) motion of the flapping member, rad
θ = rotations of beam nodes, rad
θ_{af} = angular coordinates of points on the airfoil circle in the complex plane
λ = inflow states, m/s
λ_0 = inflow velocities, m/s
ξ, η = Cartesian coordinates (for different frames)
ρ = air density, kg/m^3
Φ = commanded pitch -type motion of the flapping member, rad
χ = parameter determined by airfoil thickness and camber, $\chi = (\tau - i\sigma)/R_{af}$
Ψ = commanded roll-type (flap) motion of the flapping members, rad
$\Omega_{\zeta_B}(\beta)$ = coefficient matrix of the quaternion equations, a function of body angular velocities

Subscripts

af = airfoil
B = reference to the B frame
BB, *BF* = components of a matrix with respect to body/flexible differential equations of motion
F = reference to the flexible degrees of freedom
FB, *FF* = components of a matrix with respect to flexible/body differential equations of motion
fs = reference to free stream
hb = h vector with respect to the motion of the B frame
hε = h vector with respect to the strain ε
lv = leading-edge vortices
mc = mid-chord
pb = nodal position with respect to the motion of the B frame
pε = nodal position with respect to the strain ε

us	=	reference to the unsteady motion of airfoil
w	=	reference to the *w* frame
wk	=	wake vortices
x, *y*, *z*	=	directions of base vectors of a reference frame
θb	=	nodal rotation with respect to the motion of the *B* frame
$\theta \varepsilon$	=	nodal rotation with respect to the strain ε

I. Introduction

THE rise and growth of flapping wing Micro Air Vehicles (MAVs) have been stimulated by the long history of natural flight studies. These vehicles have the potential to revolutionize people's capabilities of gathering information in environmental monitoring, homeland security, and other time sensitive areas. Some studies have been conducted to investigate the lift generation mechanisms of flapping wings. Ref. 1 provided a comprehensive review of those studies. Shyy et al.[2] gave a detailed summary on challenges and issues associated with the MAV aerodynamics. Different aerodynamic formulations were developed and applied for the studies of MAVs in hover or forward flight. An unsteady aerodynamic formulation for insect-like flapping wings was developed by Ansari el al.[3, 4], which was based on the nonlinear wake-integral equations that considered the effects of vortex shedding from both the airfoil's leading- and trailing-edges on lift generation. Gogulapati et al.[5] implemented this formulation and coupled with MSC.Marc for the study of the aeroelastic responses of a flapping wing. They also used this coupled formulation for analyzing flexible hawkmoth wings in hover[6].

Recently, some studies (e.g., Refs. 7-9) were performed to build a numerical framework to facilitate the aeroelastic simulations of MAVs' flapping and flexible wings at variable fidelity levels. These works were focused on the interactions between the fluids and the flapping elastic wings. The framework originally involved a finite-volume Navier-Stokes fluid dynamics solver and a finite-element structural dynamic solver based on geometrically nonlinear composite beam deformations. Different CFD/CSD coupling schemes were also included in the framework. In Ref. 8, the structural dynamic solver was updated with the application of a co-rotational shell finite-element, suitable for simulating shell-like flapping wings. With the introduced computational framework, Aono et al.[10] studied the impact of spanwise flexibility on flapping wing aerodynamics for a rectangular wing with pure plunging motions. With the comparison to the experimental work performed by Heathcote et al.[11], they were able to obtain good agreement between the numerical results and the experimental data, in terms of instantaneous vertical tip displacement and thrust force on the flexible wing. They also summarized some thrust generation mechanisms with the spanwise flexibility of the wing.

In the above studies, high-fidelity formulations were used to model the flapping wing aeroelasticity, which could provide more details about the load distributions on the lift wings. On the other hand, the coupled aeroelastic and flight dynamic characteristics of these flapping wing vehicles are still an open topic to study.

In literature, there have been some investigations focused on coupled aeroelasticity and flight dynamics of aircraft with non-flapping wings. Van Schoor et al.[12] studied aeroelastic characteristics and control of highly flexible aircraft. They used linearized modes including rigid-body modes to predict the stability of the aircraft under different flight conditions. Their results indicated that unsteady aerodynamics and flexibility of the aircraft should be considered so as to correctly model the dynamic system. Patil et al.[13] studied the aeroelasticity and flight dynamics of HALE (high-altitude long-endurance) aircraft. They concluded that the large wing deformations due to the high-aspect-ratio structure may change the aerodynamic load distributions compared to the initial shape. This may bring significant changes to the aeroelastic and flight dynamic behaviors of the wings and overall aircraft. Therefore nonlinear formulations were required for analyzing the aeroelastic behaviors of these vehicles.

Gao et al.[14] studied the longitudinal dynamic stability of a hovering hawkmoth-type flapping wing MAV. In their work, aerodynamic sensitivities were evaluated based on CFD calculations of the aerodynamic loads. Eigenvalue analysis was carried out with the linearized system equations. They reported that the flapping wing model in that study was inherent dynamically stable without active controls. In contrast, Sun and Xiong[15] indicated a dynamically unstable mode using a similar solution technique, while a different wing and body kinematics.

For the nonlinear modeling and analysis of highly flexible wings and aircraft, a strain-based approach was introduced by Cesnik and Brown[16, 17]. It involved a low-order formulation that was capable of assessing the importance of structural nonlinear effects in a computationally effective manner, aimed at conceptual/preliminary vehicle design and control synthesis. In Ref. 17, HALE aircraft were modeled using a rigid fuselage and highly flexible high-aspect-ratio wings. The strain-based beam formulation was solved in the time domain using an explicit integration scheme, in order to obtain the flight dynamic response. Cesnik and Su[18, 19] extended the above work by

considering the flexibility of the fuselage and vertical tails. Stability and roll maneuverability (using the aileron deflections only) were compared for models with different flexibility levels. Shearer and Cesnik[20, 21] completed the nonlinear flight dynamic equations in the strain-based beam formulation and updated the integration scheme with an implicit, modified Newmark method, which could provide long term numerical integration stability, compared to the previous explicit method.

More recently, Su and Cesnik[22] performed the fully nonlinear analysis to study the time-domain characteristics of a flapping wing MAV. The interactions between the wing flapping kinematics and the vehicle flight dynamic response were observed from the simulation with symmetric wing flapping motions. With the free flight condition, the rigid-body motion of the vehicle could affect the local angle of attack of the airfoils and increase the stall margin. On the other side, the periodic wing flapping brought periodic pitching motion to the rigid body. The interaction significantly altered the trajectory of the vehicle. In this work, vehicle maneuver was achieved through asymmetric wing flapping actuations.

The unsteady aerodynamics employed in Ref. 22 is an implementation of the finite-state inflow theory[23-25], which has no capability to consider the leading-edge vortex shedding of the flapping wings when flow separation happens. However, the flow separation at leading-edge is highly possible, especially for flights with low Reynolds numbers. The shed vortices from the leading-edge may interact with the airfoil and affect the generated aerodynamic loads. Therefore, an unsteady aerodynamic formulation is necessary to consider this situation. In this paper, the finite-state inflow formulation used in Ref. 22 will be compared to a formulation considering discrete vortex shedding from both the leading-edge and trailing-edge of the flapping wings[3, 4]. With this implemented, the developed framework can be further served as a platform to test different aerodynamic formulations for flapping wing MAVs.

II. Theoretical Formulations

Due to the interaction between flight dynamics and aeroelastic responses, the formulation includes six rigid-body and multiple flexible degrees of freedom. The structural members are allowed fully coupled three-dimensional bending, twisting, and extensional deformations. Two types of unsteady aerodynamic formulations will be incorporated for loads on all lifting surfaces. All these formulations are implemented in Matlab and called the University of Michigan's Nonlinear Aeroelastic Simulation Toolbox (UM/NAST). An overview of the formulations implemented in UM/NAST is described below.

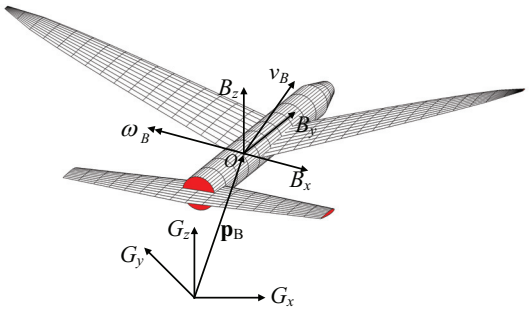

Figure 1. Global and body frames (for flight dynamics of the vehicle).

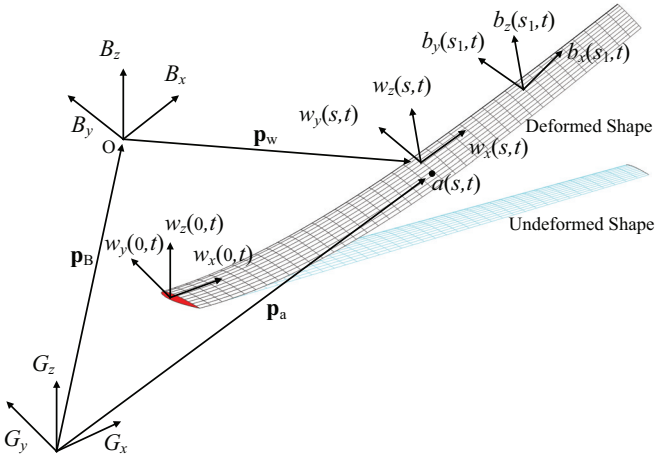

Figure 2. Flexible lifting surface frames within the body frame.

A. Fundamental Descriptions

As shown in Fig. 1, a global (inertial) frame G is defined, which is fixed on the ground. A body frame B is built in the global frame to describe the vehicle position and orientation, with B_x pointing to the right wing, B_y pointing

forward, and B_z being cross product of B_x and B_y. The position and orientation (b) and the time derivatives ($\dot{b}$ and $\ddot{b}$) of the B frame can be defined as

$$b = \begin{bmatrix} p_B \\ \theta_B \end{bmatrix}, \qquad \dot{b} = \beta = \begin{bmatrix} \dot{p}_B \\ \dot{\theta}_B \end{bmatrix} = \begin{bmatrix} v_B \\ \omega_B \end{bmatrix}, \qquad \ddot{b} = \dot{\beta} = \begin{bmatrix} \ddot{p}_B \\ \ddot{\theta}_B \end{bmatrix} = \begin{bmatrix} \dot{v}_B \\ \dot{\omega}_B \end{bmatrix} \tag{1}$$

where p_B and θ_B are the body position and orientation, both resolved in the body frame (B). Note that the origin of the body frame does not have to be the location of the vehicle's center of gravity.

As described in Fig. 2, a local beam frame (w) is built within the body frame, which is used to define the position and orientation of each node along the beam reference line. w_x, w_y, and w_z are base vectors of the beam frame, whose directions are pointing along the beam reference axis, toward the leading-edge, and normal to the beam surface, respectively, resolved in the body frame.

To model the elastic deformation of slender beams, a new nonlinear beam element was developed in the work of Ref. 17. Each of the elements has three nodes and four local strain degrees of freedom (ε), which are extension, twist, and two bending curvatures of the beam reference line.

Positions and orientations of each node along the beam are defined by a vector consisting of 12 components, which is denoted as

$$h(s)^T = \left[\left(p_B + p_w(s) \right)^T, \quad w_x(s)^T, \quad w_y(s)^T, \quad w_z(s)^T \right] \tag{2}$$

where, p_w is the position of w frame resolved in the B frame. The derivative and variation of the dependent variable h are related with those of the independent ones (ε and b).

$$\begin{aligned} \delta h &= J_{h\varepsilon}\delta\varepsilon + J_{hb}\delta b & \dot{h} &= J_{h\varepsilon}\dot{\varepsilon} + J_{hb}\dot{b} = J_{h\varepsilon}\dot{\varepsilon} + J_{hb}\beta \\ dh &= J_{h\varepsilon}d\varepsilon + J_{hb}db & \ddot{h} &= J_{h\varepsilon}\ddot{\varepsilon} + \dot{J}_{h\varepsilon}\dot{\varepsilon} + J_{hb}\dot{\beta} + \dot{J}_{hb}\beta \end{aligned} \tag{3}$$

where

$$J_{h\varepsilon} = \frac{\partial h}{\partial \varepsilon} \qquad J_{hb} = \frac{\partial h}{\partial b} \tag{4}$$

which are Jacobians obtained from kinematics[16, 18, 21].

B. Wing Flapping Kinematics

To model the wing flapping kinematics (see Fig. 3), the relative rigid-body flapping motion between the base (non-flapping) member and the attached rotating (flapping) member can be described using Euler angles. The rotation matrix R_φ between flapping and non-flapping members is obtained from the direction cosines between the two members

$$R_\varphi = \begin{bmatrix} \cos\Theta & -\sin\Theta & 0 \\ \sin\Theta & \cos\Theta & 0 \\ 0 & 0 & 1 \end{bmatrix} \begin{bmatrix} \cos\Psi & 0 & \sin\Psi \\ 0 & 1 & 0 \\ -\sin\Psi & 0 & \cos\Psi \end{bmatrix} \begin{bmatrix} 1 & 0 & 0 \\ 0 & \cos\Phi & -\sin\Phi \\ 0 & \sin\Phi & \cos\Phi \end{bmatrix} \tag{5}$$

where Θ, Φ, and Ψ are the yaw (sweeping), pitching, and roll (flapping) angles describing the rotations.

The rotational angular velocities and accelerations can be obtained from the above rotation matrix. When these Euler angles are small, the angular velocity about the local axis is approximately equal to the Euler angle rates. However, this relation does not hold for large rotation angles. In the current work, the angular velocity and accelerations are obtained through the following equations[26]

$$\boldsymbol{\omega} = \begin{bmatrix} \omega_x \\ \omega_y \\ \omega_z \end{bmatrix} = \begin{bmatrix} \dot{\Phi}\cos\Psi\cos\Theta - \dot{\Psi}\sin\Theta \\ \dot{\Phi}\cos\Psi\sin\Theta + \dot{\Psi}\cos\Theta \\ \dot{\Theta} + \dot{\Phi}\sin\Psi \end{bmatrix} = \begin{bmatrix} 0 & \cos\Psi\cos\Theta & -\sin\Theta \\ 0 & \cos\Psi\sin\Theta & \cos\Theta \\ 1 & \sin\Psi & 0 \end{bmatrix} \begin{bmatrix} \dot{\Theta} \\ \dot{\Phi} \\ \dot{\Psi} \end{bmatrix}$$

$$\dot{\boldsymbol{\omega}} = \begin{bmatrix} \dot{\omega}_x \\ \dot{\omega}_y \\ \dot{\omega}_z \end{bmatrix} = \begin{bmatrix} \ddot{\Phi}\cos\Psi\cos\Theta - \dot{\Phi}\dot{\Psi}\sin\Psi\cos\Theta - \dot{\Theta}\dot{\Phi}\cos\Psi\sin\Theta - \ddot{\Psi}\sin\Theta - \dot{\Theta}\dot{\Psi}\cos\Theta \\ \ddot{\Phi}\cos\Psi\sin\Theta - \dot{\Phi}\dot{\Psi}\sin\Psi\sin\Theta + \dot{\Theta}\dot{\Phi}\cos\Psi\cos\Theta + \ddot{\Psi}\cos\Theta - \dot{\Theta}\dot{\Psi}\sin\Theta \\ \ddot{\Theta} + \ddot{\Phi}\sin\Psi + \dot{\Phi}\dot{\Psi}\cos\Psi \end{bmatrix} \tag{6}$$

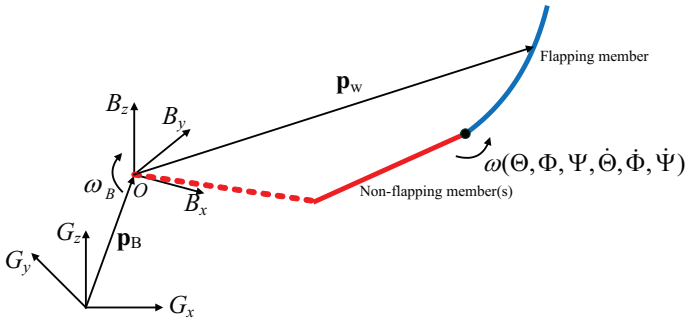

Figure 3. Kinematics relation between flapping and non-flapping members.

C. Equations of Motions

The equations of motion of the system are obtained by applying the Principle of Virtual Work. Following the same process described in Ref. 27, the elastic system equations of motion are derived as

$$\begin{bmatrix} M_{FF} & M_{FB} \\ M_{BF} & M_{BB} \end{bmatrix} \begin{bmatrix} \ddot{\varepsilon} \\ \dot{\beta} \end{bmatrix} + \begin{bmatrix} C_{FF} & C_{FB} \\ C_{BF} & C_{BB} \end{bmatrix} \begin{bmatrix} \dot{\varepsilon} \\ \beta \end{bmatrix} + \begin{bmatrix} K_{FF} & 0 \\ 0 & 0 \end{bmatrix} \begin{bmatrix} \varepsilon \\ b \end{bmatrix} = \begin{bmatrix} R_F \\ R_B \end{bmatrix} \tag{7}$$

where the generalized inertia, damping, stiffness, and force vector are

$$\begin{aligned} M_{FF}(\varepsilon) &= J_{h\varepsilon}^T M J_{h\varepsilon} & M_{FB}(\varepsilon) &= J_{h\varepsilon}^T M J_{hb} \\ M_{BF}(\varepsilon) &= J_{hb}^T M J_{h\varepsilon} & M_{BB}(\varepsilon) &= J_{hb}^T M J_{hb} \\ C_{FF}(\varepsilon,\dot{\varepsilon},\beta) &= C + J_{h\varepsilon}^T M \dot{J}_{h\varepsilon} & C_{FB}(\varepsilon,\dot{\varepsilon},\beta) &= J_{h\varepsilon}^T M H_{hb} + 2 J_{h\varepsilon}^T M \dot{J}_{hb} \\ C_{BF}(\varepsilon,\dot{\varepsilon},\beta) &= J_{hb}^T M \dot{J}_{h\varepsilon} & C_{BB}(\varepsilon,\dot{\varepsilon},\beta) &= J_{hb}^T M H_{hb} + 2 J_{hb}^T M \dot{J}_{hb} \\ K_{FF} &= K \end{aligned} \tag{8}$$

$$\begin{aligned} \begin{bmatrix} R_F \\ R_B \end{bmatrix} = &\begin{bmatrix} K_{FF}\varepsilon^0 \\ 0 \end{bmatrix} + \begin{bmatrix} J_{h\varepsilon}^T \\ J_{hb}^T \end{bmatrix} Ng + \begin{bmatrix} J_{p\varepsilon}^T \\ J_{pb}^T \end{bmatrix} B_F F^{dist} + \begin{bmatrix} J_{\theta\varepsilon}^T \\ J_{\theta b}^T \end{bmatrix} B_M M^{dist} + \begin{bmatrix} J_{p\varepsilon}^T \\ J_{pb}^T \end{bmatrix} F^{pt} + \begin{bmatrix} J_{\theta\varepsilon}^T \\ J_{\theta b}^T \end{bmatrix} M^{pt} \\ &+ \begin{bmatrix} J_{h\varepsilon}^T \\ J_{hb}^T \end{bmatrix} F^{acc} + \begin{bmatrix} J_{h\varepsilon}^T \\ J_{hb}^T \end{bmatrix} F^{cen} + \begin{bmatrix} J_{h\varepsilon}^T \\ J_{hb}^T \end{bmatrix} F^{cor} + \begin{bmatrix} J_{h\varepsilon}^T \\ J_{hb}^T \end{bmatrix} F^{int} \end{aligned} \tag{9}$$

N, B_F, and B_M are the influence matrices for gravity force, distributed force, and distributed moments, respectively, coming from the numerical integration. The generalized force vector involves the effects from initial strains (ε^0), gravity fields (g), distributed forces (F^{dist}), distributed moments (M^{dist}), point forces (F^{pt}), point moments (M^{pt}). Additional inertia loads are applied to the flapping members, which include the contributions from the rotational acceleration (F^{acc}), the centrifugal force (F^{cen}), the Coriolis effects (F^{cor}), and the interactions between the rotation of the body frame and the flapping members (F^{int}), respectively. The details about these inertia loads can be found in Ref. 22. The aerodynamic forces and moments are considered as distributed loads.

D. Peters' Finite-State Inflow Theory

The distributed loads, F^{dist} and M^{dist} in Eq. (9), are divided into aerodynamic loads and user supplied loads. The unsteady aerodynamic loads used in the existing implementation are based on the 2-D finite-state inflow theory, provided by Ref. 23. The theory calculates aerodynamic loads on a thin airfoil section undergoing large motions in an incompressible, inviscid subsonic flow. The lift, moment, and drag applied on a thin 2-D airfoil section about the mid-chord are given by

$$\begin{aligned} l_{mc} &= \pi\rho b^2\left(-\ddot{z}+\dot{y}\dot{\alpha}-d\ddot{\alpha}\right)+2\pi\rho b\dot{y}^2\left[-\frac{\dot{z}}{\dot{y}}+\left(\frac{1}{2}b-d\right)\frac{\dot{\alpha}}{\dot{y}}-\frac{\lambda_0}{\dot{y}}\right] \\ m_{mc} &= 2\pi\rho b^2\left(-\frac{1}{2}\dot{y}\dot{z}-\frac{1}{2}d\dot{y}\dot{\alpha}-\frac{1}{2}\dot{y}\lambda_0-\frac{1}{16}b^2\ddot{\alpha}\right) \\ d_{mc} &= -2\pi\rho b\left(\dot{z}^2+d^2\dot{\alpha}^2+\lambda_0^2+2d\dot{\alpha}\dot{z}+2\lambda_0\dot{z}+2d\dot{\alpha}\lambda_0\right) \end{aligned} \tag{10}$$

where b is the semi-chord of the airfoil, d is the distance of the mid-chord in front of the reference axis, $-\dot{z}/\dot{y}$ (see Fig. 4) is the angle of attack that consists of the contribution from both the pitching angle and the unsteady plunging motion of the airfoil.

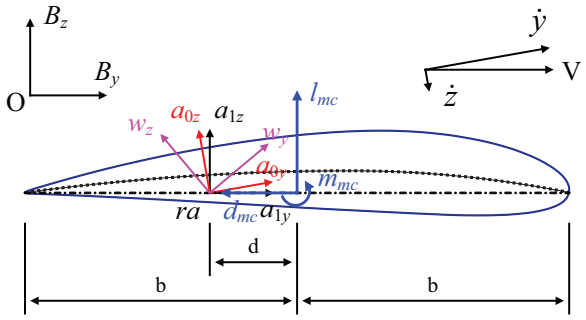

Figure 4. Airfoil coordinate system and velocity components.

The inflow velocity λ_0 is given by

$$\lambda_0 = \frac{1}{2}\sum_{n=1}^{N} b_n\lambda_n \tag{11}$$

where λ_n is the inflow states determined by the following equation

$$\dot{\lambda} = E_1\lambda + E_2\ddot{z} + E_3\ddot{\alpha} + E_4\dot{\alpha} \tag{12}$$

The coefficient matrices E_i are given in Ref. 23. b_n are obtained by the least square method[24]. Theoretically, λ_0 is an infinite summation. However, it can be approximated by letting N be between 4 and 8. Furthermore, Eq. (12) can be expressed in terms of the independent system variables by using the Jacobians

$$\dot{\lambda} = F_1\begin{bmatrix}\ddot{\varepsilon}\\ \dot{\beta}\end{bmatrix} + F_2\begin{bmatrix}\dot{\varepsilon}\\ \beta\end{bmatrix} + F_3\lambda \tag{13}$$

The loads at the mid-chord (as defined above) need to be transferred to the wing reference axis and eventually rotated to the body reference frame[27] for solving the equations of motion. Note that finite span corrections are also included in the force distribution and may come, for instance, from a CFD solution of the problem.

E. Cranfield University's Approximate Unsteady Aerodynamic Formulation

In this aerodynamic formulation, the wing is divided into several spanwise sections or airfoils and each airfoil is modeled as a continuous distribution of vorticity. The associated wakes are modeled as discrete vortices. The flow field is computed in a complex plane (see Fig. 5), where the airfoil is transferred into a circle using the conformal mapping. To map each airfoil into the circle, the generalized Joukowski transform is used

$$\zeta = Z + \frac{(1-\chi)R_{af}^2}{Z} + \frac{\chi R_{af}^3}{2Z^2} \tag{14}$$

where χ is determined by the airfoil thickness and camber parameters[3]. As indicated in Fig. 5, ζ is a frame built at the mid-chord and rotating with the airfoil. $\hat{\zeta}$ is a non-rotating frame placed at the pitching axis of the airfoil. $\tilde{\zeta}$ is a fixed (inertia) frame, where the lead-lag and plunging motions of the airfoil are defined. $\hat{\zeta}$ can be rotated from ζ, by using the instantaneous pitching angle of the airfoil (α).

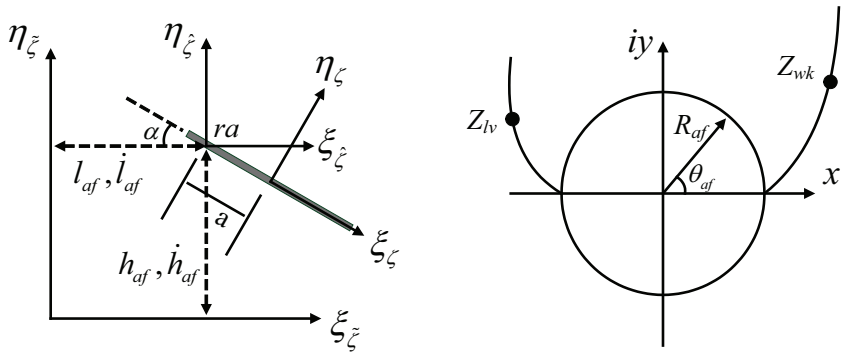

(a) Cartesian coordinate systems: airfoil rotates about its reference axis (*ra*)

(b) Complex plane

Figure 5. Transformation of aerodynamic frames.

According to Ref. 3, the bound vorticity is given as

$$\gamma_b = \gamma_0 + \gamma_1 \tag{15}$$

where γ_0 is the quasi-steady component of the bound vorticity without considering the wake effects. γ_1 accounts for the contribution from the entire wake. The quasi-steady bound vorticity is derived as

$$\gamma_0(\theta_{af}, t) = \gamma_{fs}(\theta_{af}, t) + \gamma_{us}(\theta_{af}, t) \tag{16}$$

where

$$\begin{aligned}
\gamma_{fs}(\theta_{af}, t) &= -2U_\infty \left[\sin(\theta_{af} - \alpha) + \sin\alpha\right] \\
\gamma_{us}(\theta_{af}, t) &= \frac{1}{R_{af}}\left[-A_1\cos\theta_{af} - \left(A_2 + \frac{1}{2}A_7\right)\cos 2\theta_{af} + A_3\sin\theta_{af} + \left(A_4 - \frac{1}{2}A_5 + \frac{1}{2}A_6\right)\sin 2\theta_{af}\right. \\
&\quad \left. - A_8\sin\theta_{af}\cos 2\theta_{af} + A_9\sin\theta_{af}\sin 2\theta_{af} - A_{10}\cos\theta_{af}\cos 2\theta_{af} + A_{11}\cos\theta_{af}\sin 2\theta_{af} + \frac{\Gamma_0\big|_{us}}{2\pi}\right]
\end{aligned} \tag{17}$$

θ_{af} is the angular coordinate of points on the airfoil circle in the complex plane. U_∞ is the free stream velocity aligned with the $\xi_{\tilde{\zeta}}$ axis. Definitions of A_1 to A_{11} are also given in Ref. 3. The solution of $\Gamma_0\big|_{us}$ is obtained by enforcing the Kutta condition at the trailing-edge

$$\Gamma_0\big|_{us} = 2\pi\left\{2R_{af}\left(\dot{l}_{af}\sin\alpha + \dot{h}_{af}\cos\alpha\right) + \dot{\alpha}\left[\frac{1}{2}\tau^2 + \frac{1}{2}\sigma^2 - 2R_{af}\left(R_{af}+a\right)\right]\right\} \tag{18}$$

where τ and σ are airfoil shape parameters defined in Ref. 3. Therefore, the total quasi-steady circulation can be obtained

$$\Gamma_0 = \Gamma_0\big|_{fs} + \Gamma_0\big|_{us} = 2\pi\left\{2R_{af}\left[\left(\dot{l}_{af} - U_\infty\right)\sin\alpha + \dot{h}_{af}\cos\alpha\right] + \dot{\alpha}\left[\frac{1}{2}\tau^2 + \frac{1}{2}\sigma^2 - 2R_{af}\left(R_{af}+a\right)\right]\right\} \tag{19}$$

The discrete vortices are shed from both the trailing-edge and leading-edge of the airfoil. The strengths of the shed vortices are computed by enforcing a stagnation condition at the leading-edge and a conventional Kutta condition at the trailing-edge[3]. Eq. (20) determines the strengths of the shed vortices at both edges.

$$\begin{aligned}\frac{1}{R_{af}}\left[A_1 - \left(A_2 + \frac{1}{2}A_7\right) + A_{10}\right] - 2U_\infty\sin\alpha &= \frac{1}{2\pi R_{af}}\left[\int_{wk}\Re\left(\frac{Z_{wk}-R_{af}}{Z_{wk}+R_{af}}\right)\gamma_{wk}dZ_{wk} + \int_{lv}\Re\left(\frac{Z_{lv}-R_{af}}{Z_{lv}+R_{af}}\right)\gamma_{lv}dZ_{lv}\right] \\ \Gamma_0 &= -\left[\int_{wk}\Re\left(\frac{Z_{wk}+R_{af}}{Z_{wk}-R_{af}}\right)\gamma_{wk}dZ_{wk} + \int_{lv}\Re\left(\frac{Z_{lv}+R_{af}}{Z_{lv}-R_{af}}\right)\gamma_{lv}dZ_{lv}\right]\end{aligned} \tag{20}$$

where $\Re(\bullet)$ denotes the real part of $(\bullet)$. The positions of the latest shed vortices and the strengths are unknowns in Eq. (20). The latest shed vortices are placed at specified distances from the leading-edge and trailing-edge[4]. Therefore, only γ_{wk} and γ_{lv} need to be determined. Since the positions and strengths of the vortices shed at the previous time steps are known, Eq. (20) is sufficient to determine the latest shed vortices.

The wake-induced bound vorticity on the airfoil circle is then obtained by accounting for the effects of all shed vortices in the system.

$$\gamma_1(\theta_{af},t) = -\frac{\Gamma_0}{2\pi R_{af}} - \frac{1}{2\pi R_{af}}\left[\int_{wk}\Re\left(\frac{Z_{wk}-R_{af}e^{i\theta_{af}}}{Z_{wk}+R_{af}e^{i\theta_{af}}}\right)\gamma_{wk}dZ_{wk} + \int_{lv}\Re\left(\frac{Z_{lv}-R_{af}e^{i\theta_{af}}}{Z_{lv}+R_{af}e^{i\theta_{af}}}\right)\gamma_{lv}dZ_{lv}\right] \tag{21}$$

The aerodynamic loads on each airfoil section are computed from the vorticity by using Kelvin's vortex impulse theorem, where the force and moment are obtained by computing the impulse and moment of impulse of the total vorticity in the airfoil-wake system[3]. The force and moment in the non-rotating frame ($\hat{\zeta}$) are computed as follows

$$\begin{aligned}\hat{F} &= i\rho\left[\frac{d}{dt}\oint_{af}\hat{\zeta}\gamma_0(\hat{\zeta})d\hat{\zeta} + \frac{d}{dt}\oint_{af}\hat{\zeta}\gamma_1(\hat{\zeta})d\hat{\zeta} + \frac{d}{dt}\int_{wk}\hat{\zeta}\gamma_{wk}(\hat{\zeta})d\hat{\zeta} + \frac{d}{dt}\int_{lv}\hat{\zeta}\gamma_{lv}(\hat{\zeta})d\hat{\zeta}\right] \\ \hat{M} &= \frac{\rho}{2}\left[\frac{d}{dt}\oint_{af}\left|\hat{\zeta}\right|^2\gamma_0(\hat{\zeta})d\hat{\zeta} + \frac{d}{dt}\oint_{af}\left|\hat{\zeta}\right|^2\gamma_1(\hat{\zeta})d\hat{\zeta} + \frac{d}{dt}\int_{wk}\left|\hat{\zeta}\right|^2\gamma_{wk}(\hat{\zeta})d\hat{\zeta} + \frac{d}{dt}\int_{lv}\left|\hat{\zeta}\right|^2\gamma_{lv}(\hat{\zeta})d\hat{\zeta}\right] \\ &\quad -\Im\left[i\rho U_0\left(\oint_{af}\hat{\zeta}\gamma_0(\hat{\zeta})d\hat{\zeta} + \oint_{af}\hat{\zeta}\gamma_1(\hat{\zeta})d\hat{\zeta} + \int_{wk}\hat{\zeta}\gamma_{wk}(\hat{\zeta})d\hat{\zeta} + \int_{lv}\hat{\zeta}\gamma_{lv}(\hat{\zeta})d\hat{\zeta}\right)\right]\end{aligned} \tag{22}$$

where

$$U_0 = \left(-U_\infty + \dot{l}_{af}\right) + i\dot{h}_{af} \tag{23}$$

$\Im(\bullet)$ denotes the imaginary part of $(\bullet)$

F. Coupled Nonlinear Aeroelastic and Flight Dynamic System Equations of Motion

The coupled nonlinear aeroelastic and flight dynamic system equations of motion are obtained by augmenting the equations of rigid body motion and elastic deformations with the inflow equations, which can be represented as Eq. (24)[21].

$$\begin{bmatrix} M_{FF} & M_{FB} \\ M_{BF} & M_{BB} \end{bmatrix} \begin{bmatrix} \ddot{\varepsilon} \\ \dot{\beta} \end{bmatrix} + \begin{bmatrix} C_{FF} & C_{FB} \\ C_{BF} & C_{BB} \end{bmatrix} \begin{bmatrix} \dot{\varepsilon} \\ \beta \end{bmatrix} + \begin{bmatrix} K_{FF} & 0 \\ 0 & 0 \end{bmatrix} \begin{bmatrix} \varepsilon \\ b \end{bmatrix} = \begin{bmatrix} R_F \\ R_B \end{bmatrix}$$

$$\dot{\zeta}_B = -\frac{1}{2}\Omega_{\zeta_B}(\beta)\zeta_B$$

$$\dot{P}_B = \begin{bmatrix} C^{GB}(\zeta_B) & 0 \end{bmatrix} \beta \tag{24}$$

$$\dot{\lambda} = F_1 \begin{bmatrix} \ddot{\varepsilon} \\ \dot{\beta} \end{bmatrix} + F_2 \begin{bmatrix} \dot{\varepsilon} \\ \beta \end{bmatrix} + F_3 \lambda$$

where ζ_B is the quaternions describing the orientation of the body frame (B), P_B is the inertial position of the B frame, and C^{GB} is the rotation matrix from the body frame to global frame (G). Since the aerodynamic loads calculated using Eq. (22) have inherently included the unsteady effects, the inflow equation (the last one in Eq. 24) is eliminated from the system equations, when the discrete vortex formulation is used.

III. Numerical Studies

Within the framework of UM/NAST, the new implementation of the discrete vortex formulation is first validated and its correlations with the existing finite-state inflow aerodynamic formulation are then studied. Aeroelastic responses of a flexible flapping wing and a full flapping MAV are investigated using the two formulations.

A. Verification of the Implementation of the Discrete Vortex Formulation

1) Visualization of Vortices

Some validation studies on the discrete vortex method were performed in Ref. 4, one of which was to visualize the vortices shed from both the leading-edge and trailing-edge and to correlate with experiments conducted by Dickinson and Götz[28]. In the experiment, a rectangular wing with 0.05 m chord length and 0.15 m span was moving in a straight line. The wing started with the acceleration of 0.625 m/s^2, until the travelling speed reached 0.10 m/s. The speed was kept constant before the wing was suddenly stopped after travelling 0.375 m. The 3-D effects were limited in the experiment and not considered in the numerical simulations. The visualization of vortices shed from both the leading- and trailing-edges was provided in Ref. 28 for a case where the moving wing was pitched at a constant 45^o angle. The current implementation can reproduce very similar visualizations of the vortices, compared to Refs. 4 and 28, which verifies the current implementation.

2) 1-D Flapping of an Elastic Wing

Figure 6 shows a rectangular wing that was modeled in Ref. 8 using shell elements. The aeroelastic response was calculated for the wing flapping in stationary air. The prescribed motion at the wing root is given as

$$\Theta = 0 \qquad \Phi = 0 \qquad \Psi(t) = \begin{cases} 0 & t < 0 \\ 17\sin 20\pi t \quad (\text{deg}) & t \geq 0 \end{cases} \tag{25}$$

According to the method given in Ref. 8, the Reynolds number of this case is about 1.76×10^3. Experimental studies were performed at the University of Florida. The experiment setup was similar to what was described in Ref. 29. Numerical results with an equivalent 1-cosine flapping motion were presented in Ref. 8, using different coupled CFD/CSD codes, where the aerodynamic solver (STREAM) was coupled with MSC.Marc and UM/NLAMS, respectively. In the current study, this wing is modeled as an equivalent beam, where the beam-type properties are listed in Table 1. Figure 7 compares the current results using the two aerodynamic formulations with what were

provided in Ref. 8. One may find very good agreement between the current numerical results and the previous studies.

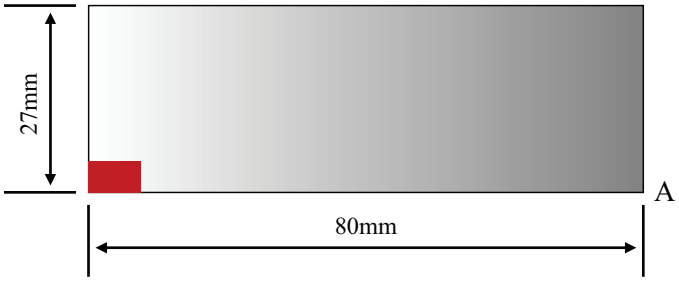

Figure 6. Rectangular flat plate flapping wing configuration with red color indicating the region on the wing that is in contact with the flapping mechanism (from Ref. 8).

Table 1. Beam-equivalent properties of the testing wing (after Ref. 8)

Length (L)	80×10^{-3}	m
Chord length (c)	27×10^{-3}	m
Mass per unit span (m)	1.46×10^{-2}	kg/m
Rotational inertia (I_{xx})	8.86×10^{-7}	kg·m
Flat bending inertia (I_{yy})	4.86×10^{-11}	kg·m
In-plane bending inertia (I_{zz})	8.86×10^{-7}	kg·m
Extensional stiffness (k_{11})	3.78×10^{5}	N
Torsional stiffness (k_{22})	1.79×10^{-3}	$N\cdot m^2$
Flat bending stiffness (k_{33})	1.26×10^{-3}	$N\cdot m^2$
In-plane bending stiffness (k_{44})	22.96	$N\cdot m^2$

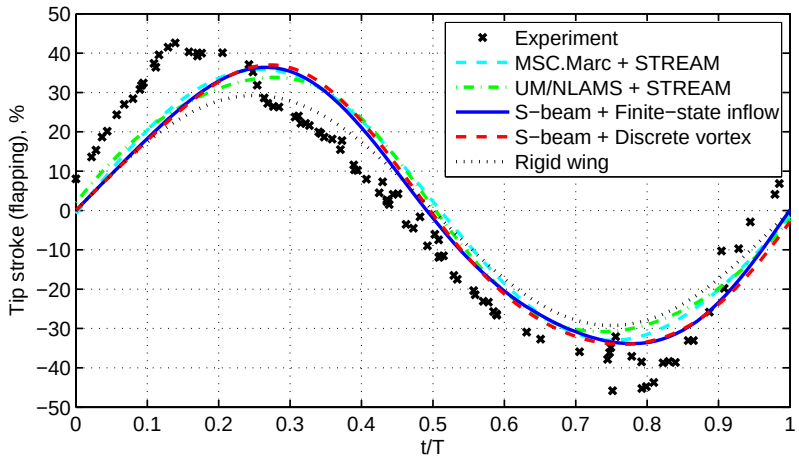

Figure 7. Wing tip stroke.

B. Correlations between the Unsteady Aerodynamic Formulations (Airfoil Level)

In this section, the two aerodynamic formulations are correlated. Both formulations are based on potential flow, and no viscous effects are included. Since the finite-state inflow theory does not consider the vortices shed from the leading-edge, attached flow are assumed when comparing the two formulations, i.e. vortices are only shed from the trailing-edge. A rigid flat plate airfoil is used for load calculations, whose chord length is 0.027 m.

1) Steady Case

The rigid airfoil is pitched at the angle of 1^o. The incoming flow velocity is 5 m/s at sea level. With such a steady case, the inflow velocities (λ_0 in Eq. 10) are not included in the calculations using the finite-state inflow theory. Thus, the wake effects are neglected and only the steady components of the aerodynamic loads are obtained. On the

other hand, wake effects are still considered in the calculations using the discrete vortex method. A time-marching simulation is performed to get the steady solution. Ideally, the results will converge to the steady solution with the time going to infinitive when the impact of wake disappears. From Fig. 8, one may find the trend of convergence in both lift and moment curves, even though neither has converged to the steady solution given by the finite-state inflow theory, within the time range of simulation. This indicates the wake effects have not disappeared yet. Different time steps are used for the time simulations using the discrete vortex method. With the time step reduced from 0.001 s to 0.0002 s, the relative errors of the lift at the end of 0.1 s are almost the same (about 3.2%). However, the moment calculation is more sensitive to the size of time steps than the lift, as the relative error is reduced from 32.7% to 3.9%. Since the calculation of aerodynamic loads in Eq. (22) is based on the time derivatives of some integrals of the whole wake systems, the discretization of the wakes is critical to get the accurate solution. This indicates the size of time steps in the simulation needs to be appropriately selected, in order to reach a good compromise between the convergent results and the solution efficiency. There were some discussions about the choice of time steps for the discrete vortex method[3]. While a uniform criterion of the size of the time steps is hard to reach, a rough estimation is used in the current work, which is give by

$$dt = \mu \frac{c}{|\bar{U}|} \tag{26}$$

where c is the chord length. $\bar{U}$ is the translational velocity of the vortex shedding point relative to the inertia frame. μ is the tuning parameter. A good compromise can be obtained when μ is about 0.05.

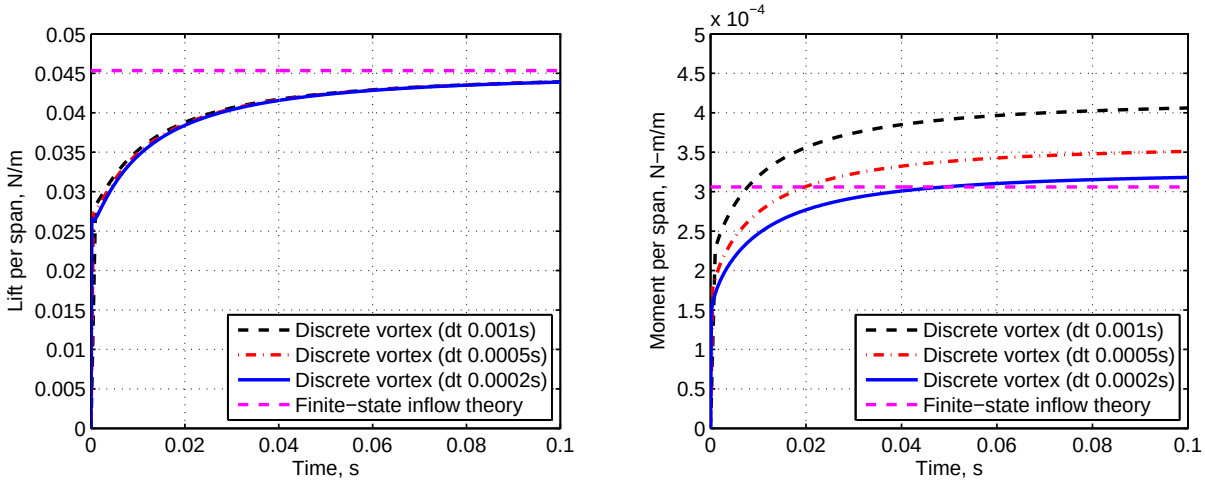

Figure 8. Steady aerodynamic lifts and moments with different time steps.

2) Unsteady Case

The airfoil is tested in a uniform flow with the free stream velocity of 5 m/s. The airfoil is subject to a sinusoidal plunging motion, which is given by

$$\dot{z}(t) = \begin{cases} 0 & t < 0 \\ -\sin 40\pi t \quad \text{(m/s)} & t \geq 0 \end{cases} \tag{27}$$

Assume there is no flow separation at the leading-edge and only the trailing-edge vortices are considered when using the discrete vortex method. The results are compared to the ones from the finite-state inflow theory in Fig. 9. Overall, the correlations are good between the two formulations. The relative errors at the peak values of lifts and moments are about 4.6% and 13.8%, respectively. Figure 10 exemplifies the shape of the wake at the trailing-edge at the end of 0.2 s.

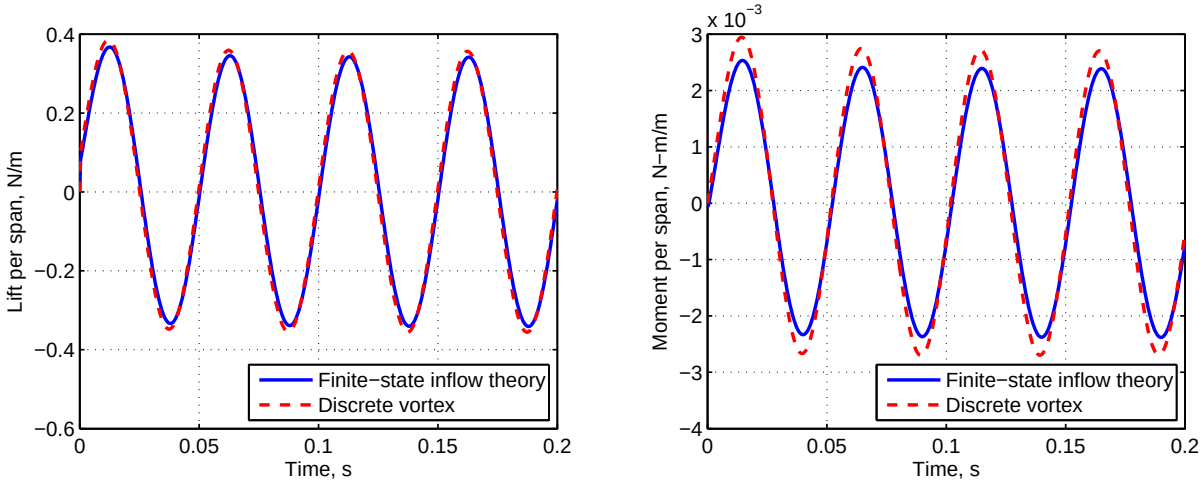

Figure 9. Airfoil lift and moment with plunging motion in a uniform flow (no leading-edge vortex shedding; plunging velocity amplitude: 1 m/s).

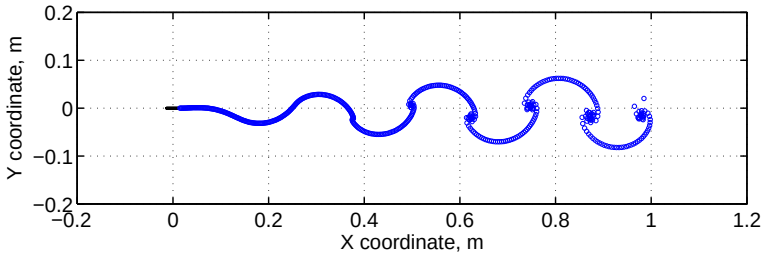

Figure 10. Visualization of wake at the end of 0.2 s using the discrete vortex method (plunging velocity amplitude: 1 m/s).

C. Airfoil Moving at High Angles of Attack

The flat plate airfoil is still used for this case. It travels within the stationary air, whose lead-lag motion features split cycles. Figure 11 exemplifies the lead-lag motion, which is determined by the combination of two cosine functions at different frequencies. The pitching angle of the airfoil is simultaneously changed in time, as shown in Fig. 12.

From the kinematics, the angle of attack of the airfoil is high to allow flow separations at the leading-edge. This phenomenon can be modeled by using the discrete vortex formulation. For comparison purpose, another simulation is performed where the attached flow is assumed. Figures 13 to 15 compare the lift, drag, and moment results in the non-rotating aerodynamic frame ($\hat{\zeta}$), with the detached and attached flow assumptions. During the forward stroke in the first cycle, the shed leading-edge vortices impact the magnitude of the aerodynamic loads in that more drag but less lift are generated on the airfoil. After the airfoil makes the first turn and starts the first backward stroke, the vortices and airfoil interact intensively, which brings some high-frequency components to the aerodynamic loads. These high-frequency loads can also be observed in the following cycles, with the presence of the preciously shed vortices.

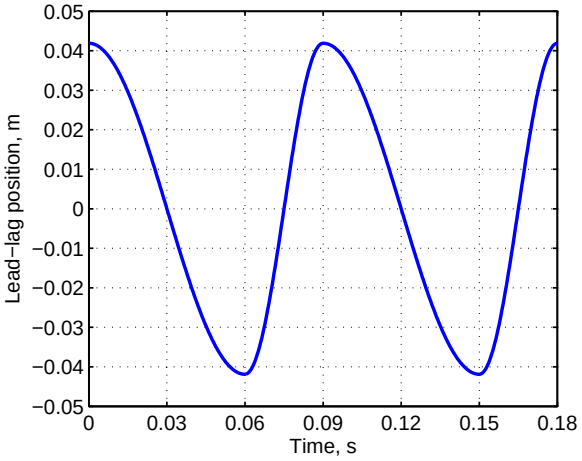

Figure 11. Lead-lag motion of the airfoil.

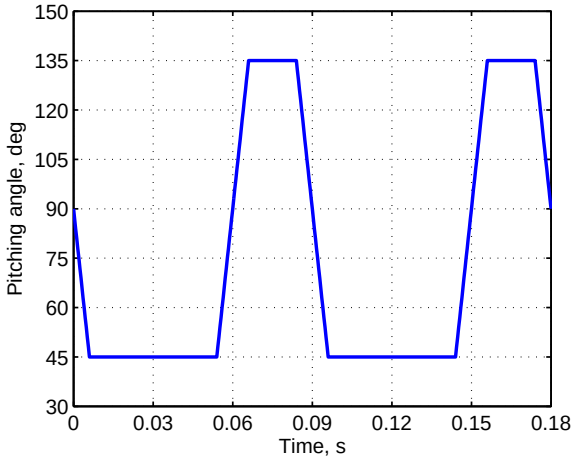

Figure 12. Pitching angle of the airfoil.

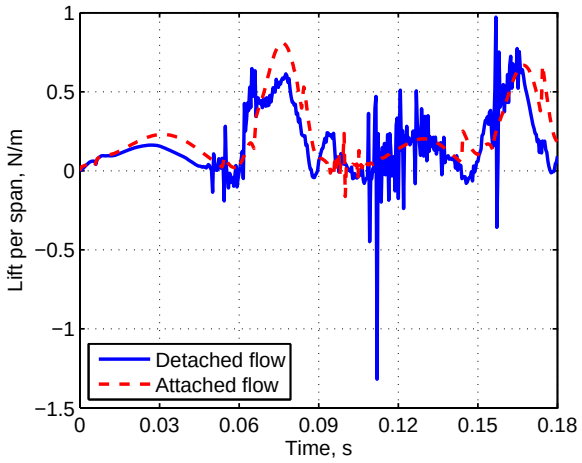

Figure 13. Impact of leading-edge vortex on lift generation.

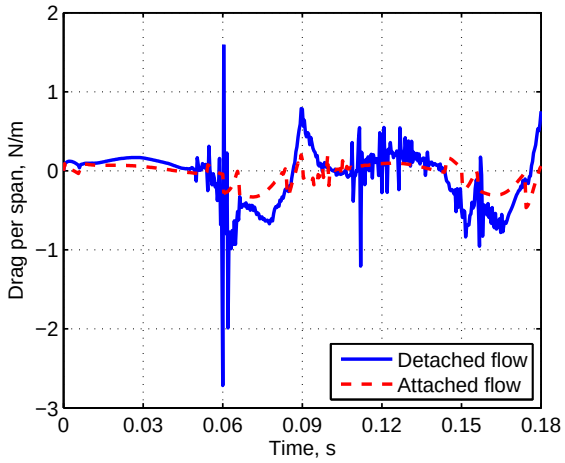

Figure 14. Impact of leading-edge vortex on drag generation.

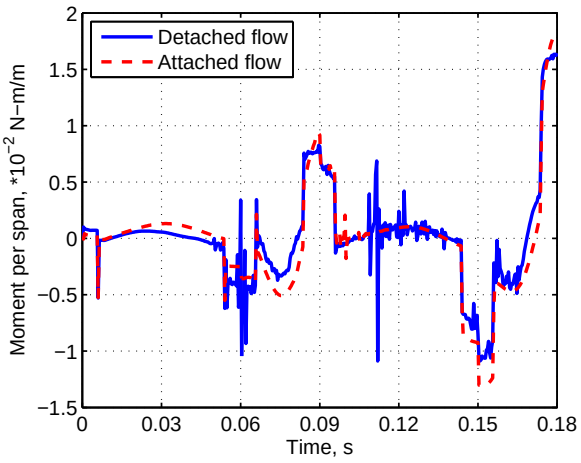

Figure 15. Impact of leading-edge vortex on moment generation.

D. Wing Flapping Simulations

Aeroelastic responses of the flexible wing used in Ref. 8 and Section A of this paper are analyzed in this section The wing root is subject to different actuations, including 1-D plunging and flapping in a uniform incoming flow.

1) Plunging of the Flexible Wing

The wing is horizontally set in air with a zero pitching angle. The flow velocity is 5 m/s at sea level. The root of the wing is subject to the sinusoidal plunging motion governed by Eq. 27. Figures 16 and 17 illustrate the lift and moment distributions obtained by using the finite-state inflow theory and the discrete vortex formulation. One may find reasonably good agreement between the two formulations, with the loads calculated using the discrete vortex method slightly higher than the finite-state inflow theory. The lift and moment distributions are not continuous between adjacent elements when using the finite-state inflow theory. This is due to the discontinuity of the inflow velocity (λ_0 in Eq. 10) between the adjacent elements. Figure 18 compares the wing tip displacement, normalized by the wing span. As expected, the discrete vortex method predicts higher displacements, particularly at some peak locations, which is corresponding to the larger loads calculated from the discrete vortex method at the same time. After all, the correlation between the two predictions is still very good with the relative error at some peaks to be about 9.1%.

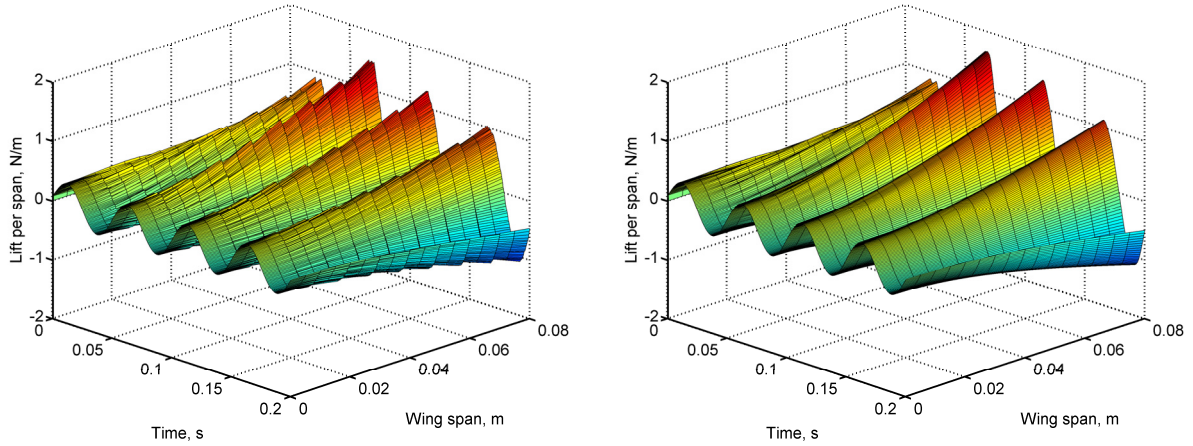

Figure 16. Lift distributions on the wing in plunging motion (left: finite-state inflow theory; right: discrete vortex method).

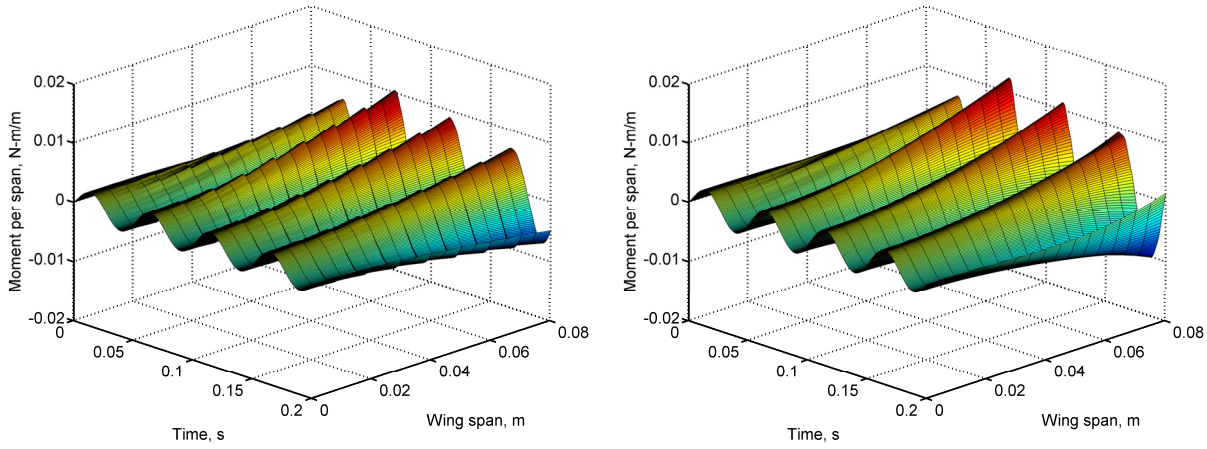

Figure 17. Moment distributions on the wing in plunging motion (left: finite-state inflow theory; right: discrete vortex method).

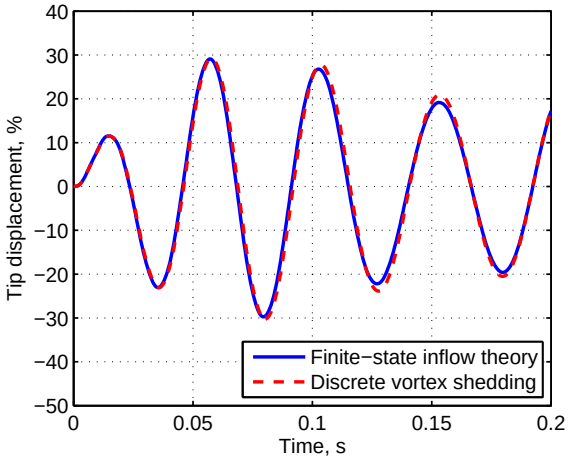

Figure 18. Tip displacement of the plunging wing (relative to wing root).

2) Flapping of the Flexible Wing

In this case, the wing is subject to a 1-D flapping actuation prescribed to the wing root, which is governed by

$$\Theta = 0 \qquad \Phi = 0 \qquad \Psi(t) = \begin{cases} 0 & t < 0 \\ 15\sin 20\pi t \quad (\text{deg}) & t \geq 0 \end{cases} \tag{28}$$

The incoming flow is still 5 m/s at sea level. With the two aerodynamic formulations applied, the lift and moment distributions are compared in Figs. 19 and 20, whereas Fig. 21 plots the wing tip strokes normalized by the wing span. Note that flow separation is also not considered in this case. From the comparisons, it is clear that the finite-state inflow formulation and the discrete vortex formulation are correlating well under this flow condition.

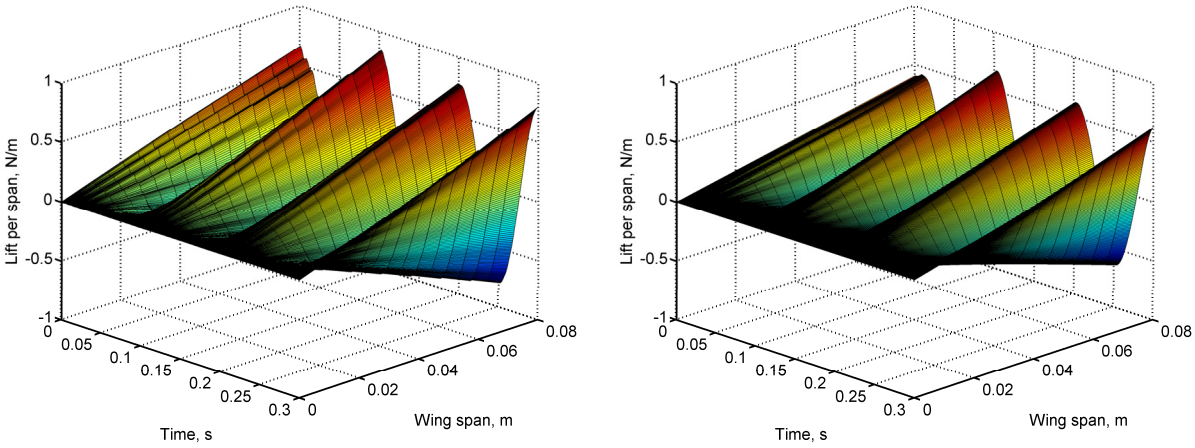

Figure 19. Lift distributions on the wing in flapping motion (left: finite-state inflow theory; right: discrete vortex method).

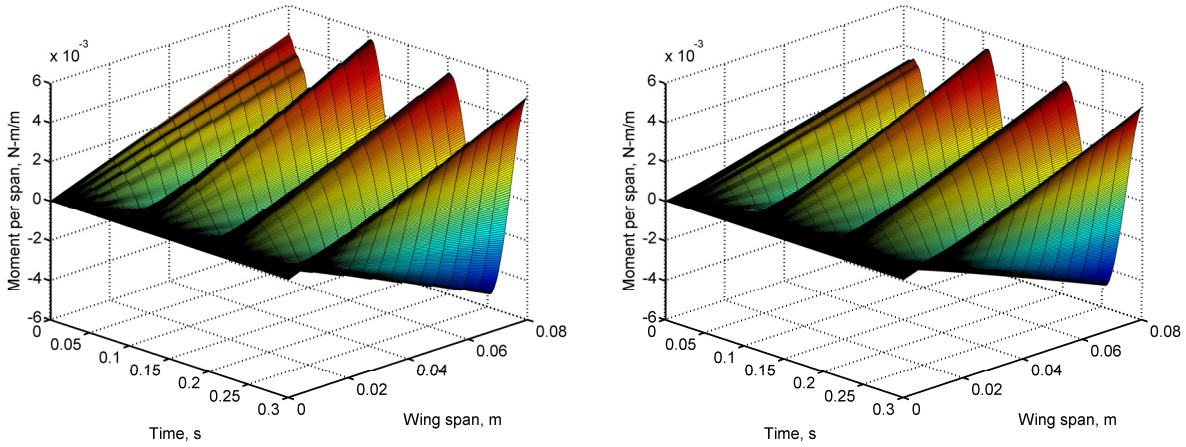

Figure 20. Moment distributions on the wing in flapping motion (left: finite-state inflow theory; right: discrete vortex method).

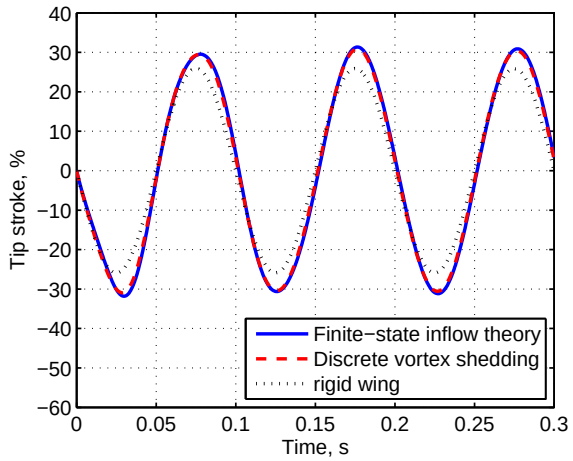

Figure 21. Tip stroke of the flapping wing in a uniform incoming flow.

3) Flapping Wing with Sweeping/Pitching Motion

In this case the wing root is prescribed with both sweeping and pitching motions in the stationary air. The sweeping angle (Θ) is defined in Fig. 22, while the pitching angle (Φ) is the same as described in Fig. 12. The Reynolds number at 75% span of the wing is about 6.10×10^3, during the backward sweeping of the wing.

Wing tip strokes normalized by the wing span are compared in Fig. 23. When the discrete vortex method is used, assumptions of both detached and attached flows are made as in the previous study. In addition, a simplified stall model[30] is applied in the simulation using the finite-state inflow formulation. When the wing starts to move, the initial pitching angle is 90°. Significant aerodynamic loads are generated in the horizontal direction, acting as drag loads to the wing. With the effects of both the drags and wing inertia, there exists an initial lag between the actual wing tip position and that of a rigid wing. As the pitching angle reduces within the stroke, the aerodynamic force tends to tilt up and more lift components are generated. Therefore, the wing is seen to bend up and begin to vibrate in the flapwise direction. After the wing makes the first turn at the end of the forward stroke, it flips back at a much faster speed, which generates larger aerodynamic loads at a higher frequency. These loads force the wing to vibrate with a larger magnitude and a higher frequency. At the end of this backward stroke, a significant overshoot of the wing tip position can be observed. The behavior in the second cycle becomes more complex with another split-cycle excitation. As indicated from the previous airfoil simulation, the loads predicted for the detached flow feature high-frequency components, especially during the second cycle of the wing motion, when more vortex/airfoil interactions can be observed than the first cycle. These high-frequency loads can alter the aeroelastic response of the wing and also bring numerical problems to the nonlinear aeroelastic simulations, where a converged solution is hard to reach

between 0.16 and 0.17 s in the second cycle. More investigations will be made to solve the problem. However, based on the available simulation results, it is evident that to include the leading-edge vortex for lift generation in such a case with flow separation is very important. The discreet vortex method with the attached flow assumption and the finite-state inflow theory with a stall correction both return the wing oscillations with large peak values in the second cycle, which indicates the aerodynamic loads calculated from these two approaches have deviated from what the discrete vortex method with detached flow predicts.

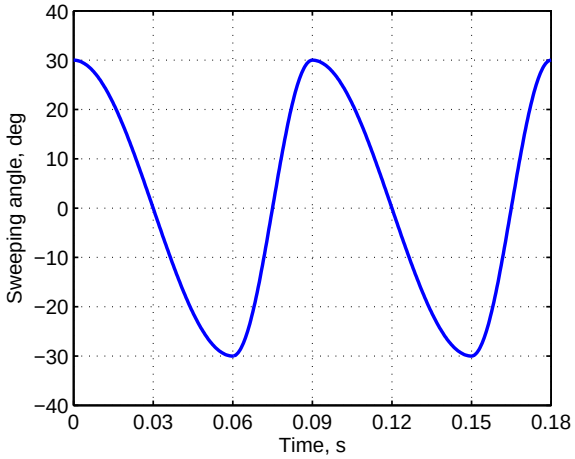

Figure 22. Sweeping angle (Θ) commanded at the wing root.

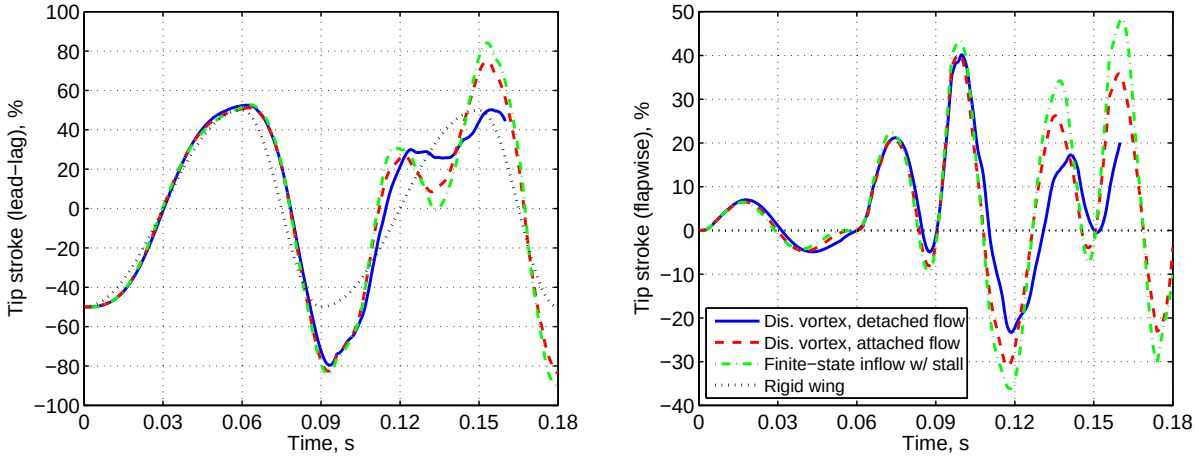

Figure 23. Wing tip strokes with the sweeping/pitching motion.

E. Coupled Aeroelastic and Flight Dynamic Simulations of a Flapping Wing MAV

The current numerical model of the full flapping wing vehicle is built based on the property of the wing analyzed in the previous section. Figure 24 shows the geometry of the full flapping wing vehicle, where the dotted lines represent the beam reference lines. Properties of the vehicle are listed in Table 2. For the main wings, the property distributions (P) along the wing span are governed by $P = P_{root}\sqrt{(L-x)/L}$, where P_{root} stands for the properties at the wing root, L is the wing span, and x is the location of a station on the wing reference line. The horizontal tail contains one elevator, as indicated in Fig. 24. This elevator occupies 25% of the chord from 25% to 75% span of the tail. A non-structural mass of 1 g is put at the front of the fuselage to adjust the c.g. location of the vehicle, which is approximately located at the pivot point of the main wings. After all, the mass ratio between the fuselage and the wings/tails is about 27.8.

The left and right wings are prescribed with the same rotations defined by

$$\Theta = 0 \qquad \Phi(t) = \begin{cases} 0 & t < 0 \\ 17\sin 20\pi t \quad (\text{deg}) & t \geq 0 \end{cases} \qquad \Psi(t) = \begin{cases} 0 & t < 0 \\ 17\sin 20\pi t \quad (\text{deg}) & t \geq 0 \end{cases} \tag{29}$$

With such a fight condition, the Reynolds number at 75% span of the wings is about 1.01×10^4, where flow field could be approximately assumed as attached throughout the flapping cycles. Therefore, the finite-state inflow theory is applicable to this simulation. The simulations start from the trimmed condition for the level flight of the vehicle without wing flapping, with a flight speed of 10 m/s at sea level. The body angle of attack is about 1.83°, and the tail elevator angle is about 5.24°.The results are compared with two other cases, one of which is free flight without wing flapping, while the other one allows the horizontal tails to flap with the following motion

$$\Theta = 0 \qquad \Phi(t) = \begin{cases} 0 & t < 0 \\ 5\sin 20\pi t \quad (\text{deg}) & t \geq 0 \end{cases} \qquad \Psi(t) = \begin{cases} 0 & t < 0 \\ 20\sin 20\pi t \quad (\text{deg}) & t \geq 0 \end{cases} \tag{30}$$

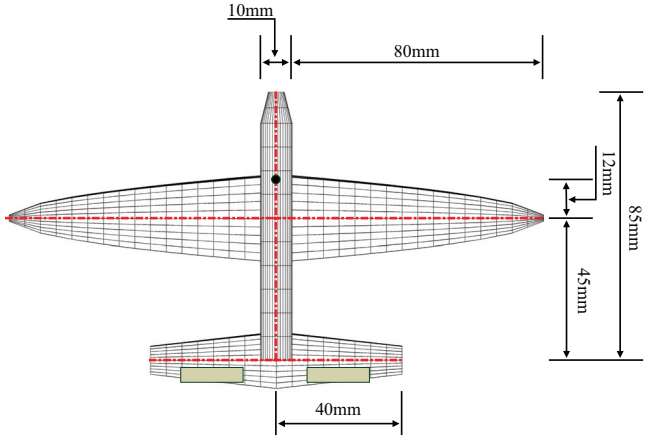

Figure 24. Geometry of the flapping wing vehicle (with no flapping actuations).

Table 2. Member properties of the flapping wing vehicle

	Wing (root)	H. Tail (root/tip)	Fuselage	Units
Ref. axis location (from L.E.)	50% chord	50% chord	50% chord	
Center of gravity (from L.E.)	50% chord	50% chord	50% chord	
Incidence angle	0	-3/-3	N/A	deg
Chord length (c)	27	18/9	10	mm
Mass per unit span (m)	2.12×10^{-3}	1.46×10^{-3}	3.16×10^{-2}	kg/m
Rotational inertia (I_{xx})	1.29×10^{-7}	8.86×10^{-8}	8.86×10^{-7}	kg·m
Flat bending inertia (I_{yy})	7.07×10^{-12}	4.86×10^{-12}	4.86×10^{-11}	kg·m
In-plane bending inertia (I_{zz})	1.29×10^{-7}	8.86×10^{-8}	8.86×10^{-7}	kg·m
Extensional stiffness (k_{11})	3.78×10^{5}	3.78×10^{5}	3.78×10^{7}	N
Torsional stiffness (k_{22})	1.79×10^{-3}	1.79×10^{-3}	1.79×10^{-1}	N·m^2
Flat bending stiffness (k_{33})	1.26×10^{-3}	1.26×10^{-3}	1.26×10^{-1}	N·m^2
In-plane bending stiffness (k_{44})	22.96	22.96	22.96×10^{2}	N·m^2

The flight path is found to be significantly affected when comparing the three cases (see Figs. 25 and 26). For the flight without wing flapping, the vehicle glides with the initial condition with no thrust force. Therefore the vehicle starts sinking right after the flight. For the vehicle with flapping wings only, the flapping of the wings initially generates more lift than the weight, which makes the vehicle climb up. However, the vehicle's pitching angle oscillates and eventually turns from positive to negative (see Fig. 27). When the pitching angle is negatively large enough, the wing flapping can no longer generate enough lift to balance the weight, and the vehicle starts to sink. The oscillation of the pitching angle of the vehicle is excited by the wing flapping, which is quite different from phugoid or short-period motions. For the vehicle with both flapping wings and tails, the tails generate additional lift in the same phase with the main wings, which results in another periodic moment about the c.g. of the

vehicle. The kinematics of the tail flapping is so chosen that the additional moment can partially balance the pitching moment caused by the flapping of the wings. Therefore, the amplitude of the pitching angle of the vehicle is reduced (see Fig. 27), compared to the vehicle with flapping wings only. The amount that the vehicle sinks at the end of 1 second is reduced, and the longitudinal distance it travels is increased corresponding. In Ref. 22, it was identified that the periodic plunging motion excited by the wing flapping could alleviate the local angle of attack on the wings. However, when the tails are allowed to flap, the alleviation is reduced, and the wing tip angle of attack becomes larger than the vehicle with only flapping wings (see Fig. 28).

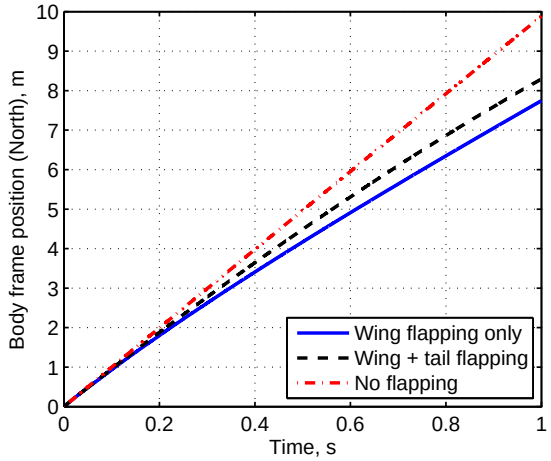

Figure 25. Body frame position (north).

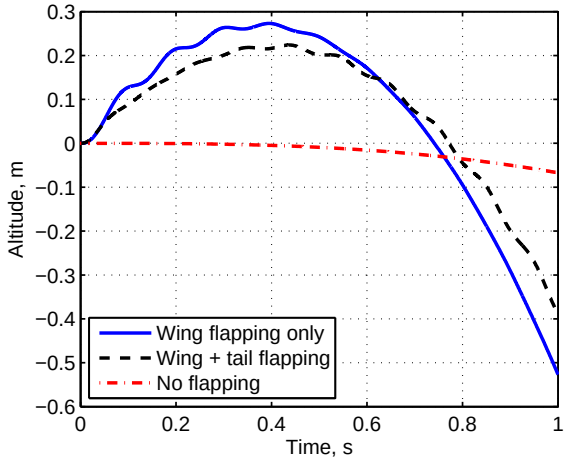

Figure 26. Altitude of the vehicle.

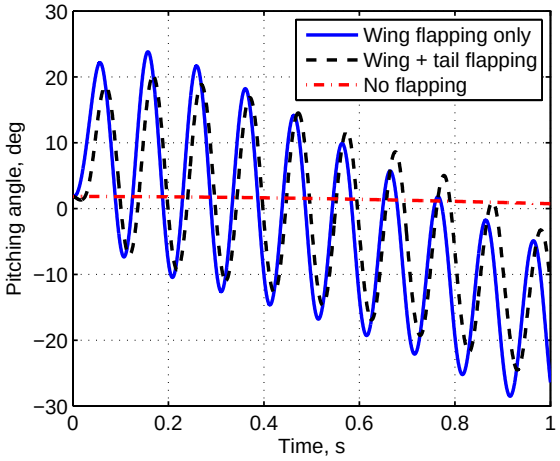

Figure 27. Body frame pitching angle.

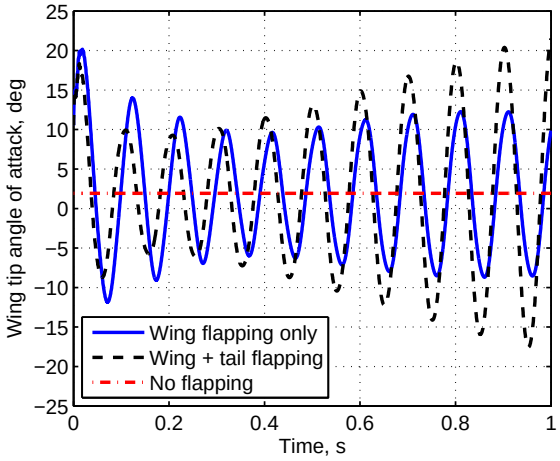

Figure 28. Angle of attack at wing tip.

IV. Conclusion

In this paper, two unsteady aerodynamic formulations were implemented for analyzing the nonlinear aeroelastic and flight dynamic characteristics of a flapping wing Micro Air Vehicle (MAV). One was Peters' finite-state inflow theory and the other was Cranfield University's discrete vortex formulation. The aerodynamic formulations were coupled with a strain-based nonlinear beam formulation for the geometrically nonlinear structural modeling and analysis. Wing flapping kinematics was described by using a set of Euler angles. Nonlinear equations of motion for the body frame attached to the vehicle (not necessarily at its c.g. point) were used to complete the coupled aeroelastic and flight dynamic formulation. Fully nonlinear analyses were performed to study the time-domain characteristics of the flapping wing MAVs with these equations implemented.

The two aerodynamic formulations were compared in this paper. When there was no flow separation at the leading-edge region, the agreement between the two aerodynamic formulations was good in terms of the calculated

aerodynamic loads of a thin flat plate airfoil. When the formulations were applied to simulations of a flexible flapping wing, very similar lift and moment distributions and aeroelastic responses of the wing were obtained for cases with no flow separations. For the case when the angle of attack was very high, the aeroelastic responses obtained from the finite-state inflow theory deviated from the results from the discrete vortex method, even when a simplified stall model was employed to adjust the aerodynamic loads.

When sweeping in the stationary air, the wing could interact with the shed vortices. This interaction was more intensive when vortices were shed from the leading-edge. Therefore, significant high-frequency aerodynamic loads were generated on the airfoil, which in turn impacted the aeroelastic responses of the flapping wing.

Coupled aeroelastic and flight dynamic responses were simulated in the framework using the finite-state inflow theory only. The tails of a full flapping wing vehicle were allowed to be flapping, in addition to the wings. Flapping actuations on the tails could reduce the oscillatory pitching motion that was induced by the wing flapping, and helped the vehicle to maintain the level flight better. However, the additional flapping motion of the tails reduced the stall margin on the wings, due to its impact on the rigid-body motions of the whole vehicle. Since the flapping kinematics of the wings/tails was pre-defined and the simulations were open-loop, a control algorithm could be set up in a close-loop to determine the appropriate wing/tail flapping motions.

To summarize, the finite-state inflow theory is suitable for flapping wing simulations, where the flow field can be considered as attached. This could be the case for relatively large birds in forward flight or hover with higher Reynolds numbers. If the Reynolds number is low due to the reduced dimension and flight speed, such as a hummingbird's flight, flow separation is significant and the leading-edge vortices play an important role in lift generation. In this case, the discrete vortex method is more suitable for the prediction of aerodynamic loads. As the computational costs increase tremendously with the number of time steps when the discrete vortex method is used, the size of time steps needs to be determined so as to compromise between the computation convergence and efficiency. Other techniques can be applied, such as vortex amalgamations suggested in Ref. 4, to reduce the computational size. At last, flow separation at an airfoil may happen periodically, during the whole flight envelop of a flapping wing MAV. Therefore, a switching point in time when the vortices start or stop shedding from the leading-edge should be established.

Acknowledgments

This work was supported by the Air Force Office of Scientific Research's Multidisciplinary University Research Initiative (MURI) grant. The authors appreciate Abhijit Gogulapati (The University of Michigan) for helping the implementation of the discrete vortex aerodynamic formulation.

References

[1]Shyy, W., Lian, Y., Tang, J., Viieru, D. and Liu, H., *Aerodynamics of Low Reynolds Number Flyers*, Cambridge University Press, New York, 2007.

[2]Shyy, W., Lian, Y., Tang, J., Liu, H., Trizila, P., Stanford, B., Bernal, L., Cesnik, C. E. S., Friedmann, P. P. and Ifju, P., "Computational Aerodynamics of Low Reynolds Number Plunging, Pitching and Flexible Wings for MAV Applications," AIAA-2008-0523, *46th AIAA Aerospace Sciences Meeting and Exhibit*, Reno, NV, Jan. 7-10, 2008.

[3]Ansari, S. A., Żbikowski, R. and Knowles, K., "Non-linear Unsteady Aerodynamic Model for Insect-Like Flapping Wings in Hover. Part 1: Methodology and Analysis," *Proceedings of the Institution of Mechanical Engineers, Part G: Journal of Aerospace Engineering* Vol. 220, No. 2, 2006, pp. 61-83.

[4]Ansari, S. A., Żbikowski, R. and Knowles, K., "Non-linear Unsteady Aerodynamic Model for Insect-Like Flapping Wings in Hover. Part 2: Implementation and Validation," *Proceedings of the Institution of Mechanical Engineers, Part G: Journal of Aerospace Engineering* Vol. 220, No. 3, 2006, pp. 169-186.

[5]Gogulapati, A., Friedmann, P. P. and Shyy, W., "Nonlinear Aeroelastic Effects in Flapping Wing Micro Air Vehicles," AIAA-2008-1817, *49th AIAA / ASME / ASCE / AHS / ASC Structures, Structural Dynamics, and Materials Conference*, Schaumburg, IL, Apr. 7-10, 2008.

[6]Gogulapati, A., Friedmann, P. P. and Shyy, W., "Approximate Aeroelastic Analysis of Flapping Wings in Hover," IFASD-2009-143, *CEAS / AIAA / DGLR International Forum on Aeroelasticity and Structural Dynamics, 2009*, Seattle, Washington, June 21-25, 2009.

[7]Tang, J., Chimakurthi, S., Palacios, R., Cesnik, C. E. S. and Shyy, W., "Computational Fluid-Structure Interaction of a Deformable Flapping Wing for Micro Air Vehicle Applications," AIAA-2008-0615, *46th AIAA Aerospace Sciences Meeting and Exhibit*, Reno, NV, Jan. 7-10, 2008.

[8]Chimakurthi, S. K., Stanford, B. K., Cesnik, C. E. S. and Shyy, W., "Flapping Wing CFD/CSD Aeroelastic Formulation Based on a Corotational Shell Finite Element," AIAA-2009-2412, *50th AIAA / ASME / ASCE / AHS / ASC Structures, Structural Dynamics, and Materials Conference*, Palm Springs, CA, May 4-7, 2009.

[9]Chimakurthi, S. K., Tang, J., Palacios, R., Cesnik, C. E. S. and Shyy, W., "Computational Aeroelasticity Framework for Analyzing Flapping Wing Micro Air Vehicles," *AIAA Journal*, Vol. 47, No. 8, 2009, pp. 1865-1878.

[10]Aono, H., Chimakurthi, S. K., Cesnik, C. E. S., Liu, H. and Shyy, W., "Computational Modeling of Spanwise Flexibility Effects on Flapping Wing Aerodynamics," AIAA-2019-1270, *47th AIAA Aerospace Sciences Meeting Including the New Horizons Forum and Aerospace Exposition*, Orlando, FL, Jan. 5-8, 2009.

[11]Heathcote, S., Wang, Z. and Gursul, I., "Effect of Spanwise Flexibility on Flapping Wing Propulsion," *Journal of Fluids and Structures*, Vol. 24, No. 2, 2008, pp. 183-199.

[12]Van Shoor, M. C., Zerweckh, S. H. and von Flotow, A. H., "Aeroelastic Stability and Control of a Highly Flexible Aircraft," AIAA-89-1187, *Proceedings of 30th AIAA / ASME / ASCE / AHS / ASC Structures, Structural Dynamics and Materials Conference*, Mobile, AL, Apr. 3-5, 1989.

[13]Patil, M. J., Hodges, D. H. and Cesnik, C. E. S., "Nonlinear Aeroelasticity and Flight Dynamics of High-Altitude Long-Endurance Aircraft," *Journal of Aircraft*, Vol. 38, No. 1, 2001, pp. 88-94.

[14]Gao, N., Aono, H. and Liu, H., "A Numerical Analysis of Dynamic Flight Stability of Hawkmoth Hovering," *Journal of Biomechanical Science and Engineering*, Vol. 4, No. 1, 2009, pp. 105-116.

[15]Sun, M. and Xiong, Y., "Dynamic Flight Stability of a Hovering Bumblebee," *Journal of Experimental Biology*, Vol. 208, No. 3, 2005, pp. 447-459.

[16]Cesnik, C. E. S. and Brown, E. L., "Modeling of High Aspect Ratio Active Flexible Wings for Roll Control," AIAA-2002-1719, *43rd AIAA / ASME / ASCE / AHS / ASC Structures, Structural Dynamics, and Materials Conference*, Denver, CO, Apr. 22-25, 2002.

[17]Cesnik, C. E. S. and Brown, E. L., "Active Wing Warping Control of a Joined-Wing Airplane Configuration," AIAA-2003-1715, *44th AIAA / ASME / ASCE / AHS / ASC Structures, Structural Dynamics, and Materials Conference*, Norfolk, VA, Apr. 7-10, 2003.

[18]Cesnik, C. E. S. and Su, W., "Nonlinear Aeroelastic Modeling and Analysis of Fully Flexible Aircraft," AIAA-2005-2169, *46th AIAA / ASME / ASCE / AHS / ASC Structures, Structural Dynamics, and Materials Conference*, Austin, TX, Apr. 18-21, 2005.

[19]Cesnik, C. E. S. and Su, W., "Nonlinear Aeroelastic Behavior of Fully Flexible Slender Vehicles," *CEAS / AIAA / DGLR International Forum on Aeroelasticity and Structural Dynamics, 2005*, Munich, Germany, Jun. 28 - Jul. 1, 2005.

[20]Shearer, C. M. and Cesnik, C. E. S., "Modified Generalized Alpha Method for Integrating Governing Equations of Very Flexible Aircraft," AIAA-2006-1747, *47th AIAA / ASME / ASCE / AHS / ASC Structures, Structural Dynamics, and Materials Conference*, Newport, RI, May 1-4, 2006.

[21]Shearer, C. M. and Cesnik, C. E. S., "Nonlinear Flight Dynamics of Very Flexible Aircraft," *Journal of Aircraft*, Vol. 44, No. 5, 2007, pp. 1528-1545.

[22]Su, W. and Cesnik, C. E. S., "Coupled Nonlinear Aeroelastic and Flight Dynamic Simulation of a Flapping Wing Micro Air Vehicle," IFASD-2009-142, *CEAS / AIAA / DGLR International Forum on Aeroelasticity and Structural Dynamics, 2009*, Seattle, Washington, June 21-25, 2009.

[23]Peters, D. A. and Johnson, M. J., "Finite-State Airloads for Deformable Airfoils on Fixed and Rotating Wings," *Symposium on Aeroelasticity and Fluid/Structure Interaction, ASME Winter Annual Meeting*, Chicago, IL, Nov. 6-11, 1994.

[24]Peters, D. A., Karunamoorthy, S. and Cao, W.-M., "Finite State Induced Flow Models Part I: Two-Dimensional Thin Airfoil," *Journal of Aircraft*, Vol. 32, No. 2, 1995, pp. 313-322.

[25]Peters, D. A., Hsieh, M.-C. A. and Torrero, A., "A State-Space Airloads Theory for Flexible Airfoils," *Journal of the American Helicopter Society*, Vol. 51, No. 4, 2007, pp. 329-342.

[26]Amirouche, F. M. L., *Computational Methods in Multibody Dynamics*, Prentice Hall, Englewood Cliffs, NJ, 1992.

[27]Su, W. and Cesnik, C. E. S., "Nonlinear Aeroelasticity of a Very Flexible Blended-Wing-Body Aircraft," AIAA-2009-2402, *50th AIAA / ASME / ASCE / AHS / ASC Structures, Structural Dynamics, and Materials Conference*, Palm Springs, CA, May 4-7, 2009.

[28]Dickinson, M. H. and Götz, K. G., "Unsteady Aerodynamic Performance of Model Wings at Low Reynolds Numbers," *Journal of Experimental Biology*, Vol. 174, No. 1, 1993, pp. 45-64.

[29]Wu, P., Stanford, B. and Ifju, P., "Passive Bending and Twisting Motion during the Flapping Stroke of a Micro Elastic Wing for Thrust Production " AIAA-2009-879, *47th AIAA Aerospace Sciences Meeting Including the New Horizons Forum and Aerospace Exposition*, Orlando, FL, Jan. 5-8, 2009.

[30]Su, W. and Cesnik, C. E. S., "Dynamic Response of Highly Flexible Flying Wings," AIAA-2006-1636, *47th AIAA / ASME / ASCE / AHS / ASC Structures, Structural Dynamics, and Materials Conference*, Newport, RI, May 1-4, 2006.